



HAL
open science

Nanoindentation of bio-sourced adhesive 75% rosin/25% beeswax: Experimental results and modelisation

Marion Girard, Yves Gaillard, Alain Burr, Evelyne Darque Ceretti, Eric Felder

► To cite this version:

Marion Girard, Yves Gaillard, Alain Burr, Evelyne Darque Ceretti, Eric Felder. Nanoindentation of bio-sourced adhesive 75% rosin/25% beeswax: Experimental results and modelisation. *Mechanics of Materials*, 2014, 69 (1), pp.185-194. 10.1016/j.mechmat.2013.10.005 . hal-02300146

HAL Id: hal-02300146

<https://hal.science/hal-02300146>

Submitted on 23 Oct 2019

HAL is a multi-disciplinary open access archive for the deposit and dissemination of scientific research documents, whether they are published or not. The documents may come from teaching and research institutions in France or abroad, or from public or private research centers.

L'archive ouverte pluridisciplinaire **HAL**, est destinée au dépôt et à la diffusion de documents scientifiques de niveau recherche, publiés ou non, émanant des établissements d'enseignement et de recherche français ou étrangers, des laboratoires publics ou privés.

Nanoindentation of bio-sourced adhesive 75% rosin/25% beeswax: Experimental results and modelisation

M. Girard ^{*}, Y. Gaillard, A. Burr, E. Darque-Ceretti, E. Felder

MINES ParisTech., CEMEF – Centre de Mise en Forme des Matériaux, CNRS UMR 7635, CS 10207, BP 207, 1 rue Claude Daunesse, 06904 Sophia Antipolis Cedex, France

A bio-sourced adhesive made of 75%w/w rosin and 25%w/w beeswax was studied in terms of tack and mechanical properties. These behaviours were highlighted by experimental nanoindentation. They depend strongly upon the applied strain rate and are moreover dictated by a “size effect” (Indentation Size Effect). The goal of this paper is to model these phenomena in order to simulate any nanoindentation test on this adhesive. At first, the dependence on strain rate and the macroscopic law of material behaviour were characterised by means of compression tests. Then the size effect was identified by inverse analysis from the nanoindentation tests by adjusting a “zoning”. And finally, a cohesive zone model was implemented to represent the tackiness of the material. The experimental measurements and the numerical results are in good agreement.

1. Introduction

With the recent increase of interest for mechanical behaviour at the nano-scale of polymers and biological matter, instrumented indentation and nanoindentation appear as powerful instruments for mechanical characterisation of adhesive behaviour (Giri et al., 2001; Yang, 2002; Sirghi and Rossi, 2006; Ebenstein and Pruitt, 2006). However, even if this mechanical test is quite simple to implement, its interpretation remains delicate. In fact, the distribution of stress around the imprint and above all the evolution of the contact area with the penetration depth are still a challenge. Analytical solutions exist only for an elastic contact of an arbitrary axisymmetric indenter (Sneddon, 1965; Pharr et al., 1992). They can even be extended for elasto-plastic contacts by following the concept of equivalent indenter shape (King, 1987; Oliver and Pharr, 1992; Bolshakov et al., 1995), as long as the unloading

behaviour can be considered as purely elastic. This is true for most of the metals and ceramics at room temperature but becomes untrue for most of the soft materials which generally exhibit viscous behaviour. By introducing a term corresponding to the adhesion energy in the Hertz solution, the JKR model was developed to answer to a spherical adhesive elastic contact (Johnson et al., 1971; Barthel, 2008). The edge of the contact can be seen as an interfacial crack that propagates during the unloading step. According to the expression of the stress intensity factor acting on the crack tip, adhesion energy and the propagation of the crack can be related. A number of authors have shown that this solution is well adapted for the indentation of viscoelastic solids (Giri et al., 2001; Barthel and Fretigny, 2009). For example, latex gives reasonable values for work of adhesion (Giri et al., 2001). More recently analytical solutions were also developed for elastic axisymmetric adhesive contact on layered media (Barthel and Perriot, 2007; Mary et al., 2006; Argatov, 2010).

However, if elastic contacts appear to be a good method to characterise adhesion, some materials do not exhibit a pure elastic behaviour at room temperature even for very low loads and using spherical indenter having a large radius of curvature. In particular, materials having a very low yield

^{*} Corresponding author. Address: Institut de Recherche en Génie Civil et Mécanique (UMR CNRS 6183), LUNAM Université, Université de Nantes, Ecole Centrale de Nantes, 58 rue Michel Ange, BP 420, 44606 Saint-Nazaire, France. Tel.: +33 272648757.

E-mail address: marion.girard@univ-nantes.fr (M. Girard).

strength (Ji et al., 2009) or, a glass transition or a melting point very close to room temperature are concerned (Kameda, 2005; Jablonski et al., 1999). Most of the waxes (Morgan et al., 2002), biological tissues (Prevost et al., 2011) or gelatines at low concentration (Kasapis and Sablani, 2005) can be cited as examples. This kind of material necessitates taking into account plasticity laws to describe fully their behaviour under nanoindentation. In this aim, numerous authors have shown that coupling experiment with finite element simulation and inverse analysis is a very powerful method in order to assess plasticity parameters but also viscous and adhesive properties (Qian et al., 2008; Qasmi et al., 2004; Keerthika et al., 2009). This present work must therefore be viewed in this context.

Rosin is an amorphous bio-sourced material, renewable and abundant. It is mainly known for its derivatives and their adhesive applications (Arizona Chemical, 2013; Eastman, 2013). In fact this material presents a very low surface tension if mixed with the correct solvent. However at room temperature, rosin is very brittle and necessitates the adding of a plasticizer to be mechanically viable. In this paper, we purpose to study the blend of rosin with beeswax. The choice of beeswax as a natural plasticizer is of course motivated by its bio-sourced aspect, but also by its miscibility with rosin to form homogeneous blends (Gaillard et al., 2011). Furthermore, it has been recently shown that beeswax improves greatly the mechanical reliability of rosin, especially through the existence of a regime of superplastic deformation for rosin concentration in the blend within 55–92 wt.% (Gaillard et al., 2013). So blends of rosin and beeswax appear as excellent candidates for combining both adhesive and plastic behaviour when deformed by nanoindentation.

We purpose to study the elasto-viscoplastic adhesive behaviour under nanoindentation of a particular beeswax/rosin blend containing 25% in weight of beeswax. The choice of this particular blend rate is motivated by the flexibility to obtain all necessary shapes for further experimental investigations.

The paper will be organised as follows. The first part is entirely devoted to the experimental work. Typical curves of nanoindentation, characteristic of an adhesive contact on a plastic material, are presented. In particular, values for the adhesion energy are deduced and a great attention has been paid to the Indentation Size Effect (ISE) very marked for this material. The second part describes the modelling and simulation of the nanoindentation tests. A constitutive law, deduced from the previous experimental observations but also from experimental compression tests, is implemented in a finite element code. We particularly insist on the implementation of the ISE observed experimentally and a cohesive zone model is used to account for the adhesive behaviour. Finally we discuss the ability of the Finite Element Model (FEM) to account for the different behaviour observed experimentally and we conclude about the nature of adhesion.

2. Material and methods

Pristine rosin and beeswax were both purchased at a professional apiarist (Ets Leygonie, 2013). They were

melted at 100 °C. The complete melting procedure has been described in a previous paper (Gaillard et al., 2013). The prepared blend has the following weight proportion: 75 wt.% of rosin and 25 wt.% of beeswax.

The nanoindentation tests were performed at room temperature with a Hysitron indenter with a Berkovich tip having a tip defect of about 250 nm radius. Indentations have been performed in open loop mode. Four constants logarithmic depth speeds were applied ($\frac{\dot{h}}{h} = 0.004, 0.04, 0.4$ and 4 s^{-1}) for the loading. An unloading time of 10 s was applied for all the tests, with constant unloading speed equal to $F_{\text{max}}/10$ where F_{max} is the maximum applied force. However, as it will be shown in the following, the response of the material is not taken into account in the control of the instrument which is not well adapted if an holding segment is added between loading and unloading part, especially in case of very viscous material. A total of 21 different tests were realised on this particular concentration of blend. The calibration of the indenter shape was performed by indenting fused silica.

The microhardness tests were performed with a Buehler indenter with a Vickers tip. A 3 g load was applied during 30 s.

Compression tests were performed with an Erichsen electromechanical apparatus. Cylindrical samples of 10 mm height and 8 mm diameter were compressed at constant strain rate. A release agent was used between the sample and the plates of the machine to reduce friction. The length of the sample is recorded in situ using a digital camera at an image acquisition frequency of 33 Hz.

3. Experimental nanoindentation tests/experimental observations

Experimental nanoindentation tests were performed following the protocol defined above. These different tests, realised with different strain rates and at different penetration depths, point out several properties of the material. These properties are studied and fully described in this section in order to model them in the following.

3.1. Influence of strain rate

The two sets of four tests, shown Fig. 1, are highlighting the strong dependence of the material at strain rate. Indeed, for the same penetration depth value during the loading ($h = 400 \text{ nm}$), the measured load evolves following a power law type with respect to the strain rate with a sensitivity coefficient of $m = 0.42$. The influence of the strain rate is largely significant and should be considered in the modelling of nanoindentation testing of this material.

This viscoplastic behaviour, observed at room temperature and which tends to a superplastic regime, was explained in Gaillard et al. (2013). The glass transition of the amorphous part of the blend and the first phase transition of the crystalline part of the blend were respectively measured at 31 °C and 38 °C (Gaillard et al., 2013). Furthermore, the complete melting of the blend is reached at 60 °C (Gaillard et al., 2013). Consequently the strain rate sensitivity

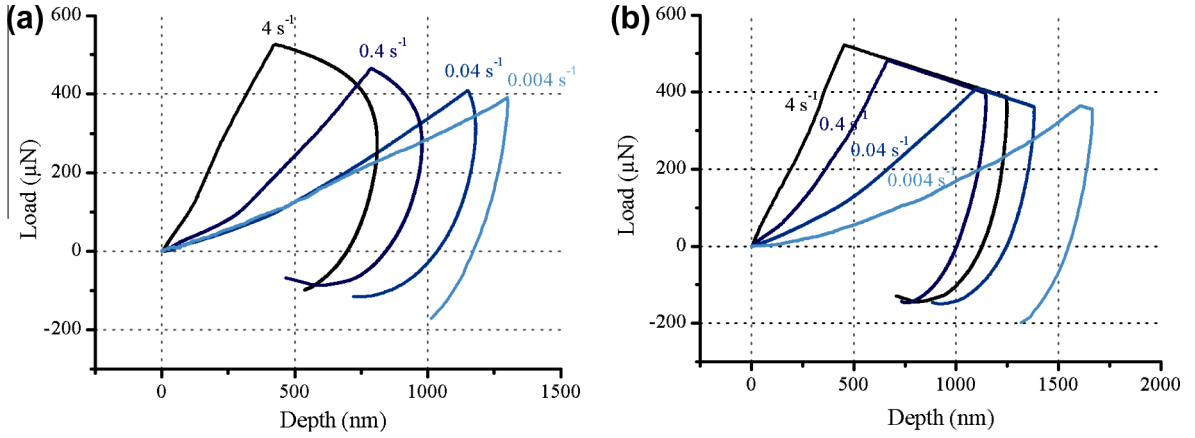


Fig. 1. Force–displacement curve of experimental nanoindentation tests at 4 different ratio $\frac{\dot{h}}{h}$: (a) nanoindentation curves obtained without holding time between loading and unloading and (b) curves obtained with a holding time of 10 s.

in the elastic but also in the plastic regime, is greatly influenced at low temperature, e.g. near room temperature.

On the nanoindentation curves (Fig. 1a), the presence of viscoplastic behaviour is revealed by a large creep during the unloading portion of the curve. Indeed, a loading rate control was used on this strain rate dependent material. The creeping rate can be higher in magnitude than the rate of elastic recovery. As a consequence the penetration depth increases during the first portion of the unloading. This nose effect (Briscoe et al., 1998) is even more important than the loading rate is high. The classical analysis of the unloading-curves by the model of Oliver and Pharr is prohibited (Oliver and Pharr, 2004). As it is generally proposed for the indentation of rate dependent solids (Ebenstein and Pruitt, 2006; Briscoe et al., 1998), holding the load between the loading and the unloading segment reduces this nose effect (Fig. 1b). However, as the instrument work here in open loop mode and as the strain rate dependency is very important ($m = 0.42$), this method cannot be retained in order to assess the mechanical properties of this material from the unloading curves. In Fig. 1b, the pseudo-holding time is 10 s.

3.2. Indentation size effect

From the experimental tests of nanoindentation an equivalent hardness was calculated with the following equation:

$$H_u = \frac{F_{\max}}{A_c} \quad (1)$$

where H_u is the equivalent hardness, F_{\max} is the maximal applied load and A_c is the projected contact surface between indenter and material at maximal load. As previously indicated the classical Oliver and Pharr procedure is not relevant for further analysis of the unloading curves. Therefore a first approximation was considered, i.e. $h \approx h_c$, where h is the total indenter displacement and h_c the contact depth (as shown on Fig. 2). A_c was analytically calculated at the maximal load ($h = h_{\max}$) considering the blunt equivalent cone of the real Berkovich indenter and its tip defect. Then the equivalent hardness for each indent can

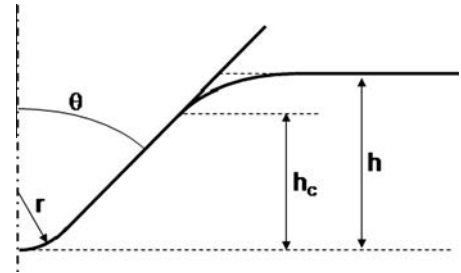


Fig. 2. Schematic representation in 2D of the nanoindentation test with a blunt equivalent cone.

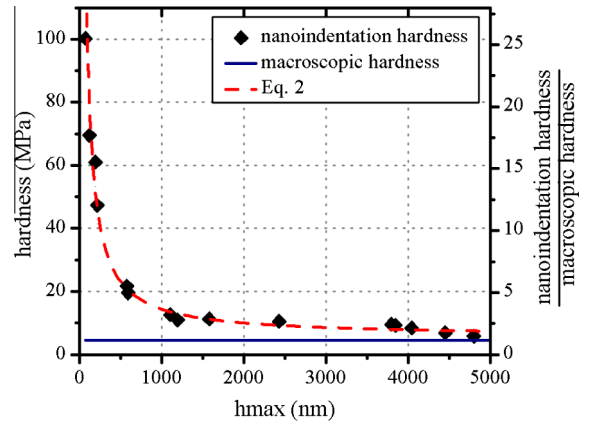


Fig. 3. Equivalent hardness H_u versus maximal indentation depth h_{\max} at $\frac{\dot{h}}{h} = 0.04 \text{ s}^{-1}$.

be calculated (Eq. (1)). This approximation will be discussed thereafter.

The calculated equivalent hardnesses at $\frac{\dot{h}}{h} = 0.04 \text{ s}^{-1}$ were plotted as a function of maximal depth h_{\max} on Fig. 3 and were compared to the macroscopic hardness H_0 measured on the same material. A significant increase in hardness is observed at lower indentation depths. The hardness ratio H_u/H_0 can reach 25 for the smallest

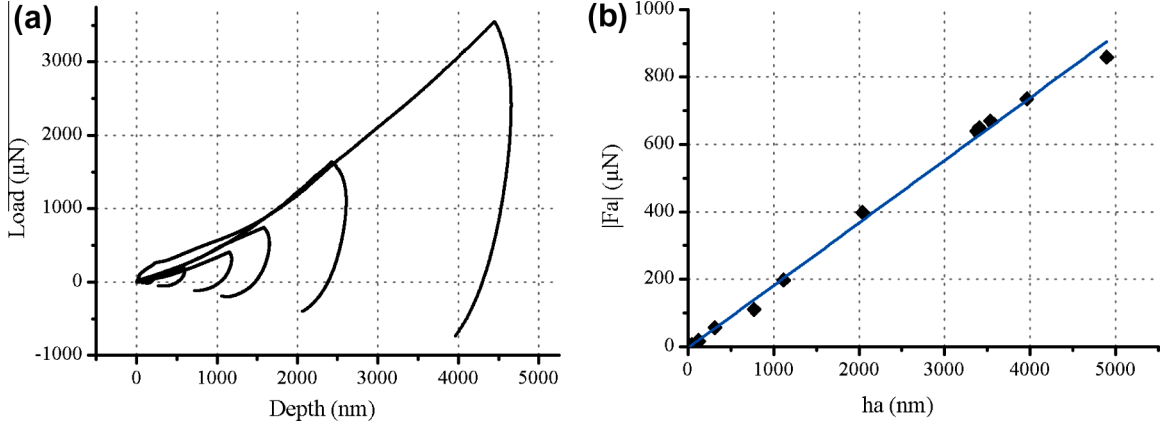


Fig. 4. (a) Nanoindentation curves obtained at $\dot{h} = 0.04 \text{ s}^{-1}$ showing the adhesion force F_a and (b) linear relationship between adhesive force F_a and the penetration depth h_a to loss of contact.

measured indent. Values of equivalent nanoindentation hardness and macroscopic hardness become similar for indentation depths greater than $5 \mu\text{m}$.

The size effect in indentation is relatively well understood for metals and ceramics and is generally associated with the presence of an internal length (grain size, distance to dislocation...) in the constitutive law of the material. For polymer materials its interpretation remains an open question and is still under investigation. Nikolov et al. (Nikolov et al., 2007; Han and Nikolov, 2007) developed a model for solid polymer based on Frank elasticity, normally used for liquid crystals. This model assumes that the size effect in polymers is due to the distinction between probing the stiffness of a single molecule and probing the interaction between the different chains composing the polymer. This model was extended by Han and Nikolov (Han and Nikolov, 2007) to the elasto-plastic behaviour (indentation) of nematic elastomers. It appears to be particularly well adapted to our blends. In fact, beeswax is a partially crystalline material with a nematic-like structure (Dorset, 1999), composed of crystalline lamellae dispersed among an amorphous matrix. Blends of rosin and beeswax also exhibit this type of structure (Gaillard et al., 2011). For this particular blend, lamellae are $5\text{--}10 \mu\text{m}$ long and $1\text{--}2 \mu\text{m}$ thick. Furthermore, at room temperature ($20 \text{ }^\circ\text{C}$), this blend is solicited very close to its glass transition, located at $31 \text{ }^\circ\text{C}$, and to the first polymorphic transformation of the crystalline part at $38 \text{ }^\circ\text{C}$ (Gaillard et al., 2011; Gaillard et al., 2013).

The tendency observed in Fig. 3 is in good agreement with the theory of Han (Han and Nikolov, 2007) and Tatiraju et al. (Tatiraju et al., 2008) (Eq. (2)).

$$H = H_0 \left(1 + \frac{c_l}{h} \right) \quad (2)$$

where c_l is a length scale parameter and H_0 is the macroscopic hardness.

H_0 and c_l were identified from Fig. 3 and Eq. (2) as $H_0 = 5.7 \text{ MPa}$ and $c_l = 0.868 \mu\text{m}$. It is interesting to note that c_l has the same order of magnitude than the typical

size of the lamellae, which compose the structure of the material.

In the same way as the dependence on the strain rate, the size effect should also be taken into account in any modelling of nanoindentation test. On this material the size effect is already important for tests with maximal penetrations below $1 \mu\text{m}$.

3.3. Tackiness

The negative force observed experimentally at the end of unloading (Fig. 4a) results from the adhesion effect between the indenter and the material. The increase of this force, called adhesive force F_a , is related to the increase of penetration depth of the indenter. It is also observed a linear relationship (Fig. 4b) between adhesive force and the penetration depth at the loss of contact, noted h_a , which was previously mentioned by Yang (Yang, 2006) and Sirghi et al. (Sirghi and Rossi, 2006).

In the flowing calculation, elastic deformation and viscous flow during the separation are neglected. We consider the energy of adhesion (Jonhson et al., 1971; Sirghi and Rossi, 2006) at the indenter-sample contact as:

$$W_a = -\gamma_a A'_c \quad (3)$$

where γ_a is the thermodynamic work of adhesion and A'_c the indenter-sample contact area.

For a perfect conical indenter with half apex angle θ and considering $h \approx h_c$, it is possible to calculate A'_c , depending on h , with the following equation:

$$A'_c(h) = \frac{\pi \tan \theta}{\cos \theta} h^2. \quad (4)$$

Use of Eq. (5), applied for $h = h_a$, in Eq. (3) gives a new expression for the contact adhesion energy:

$$W_a = -\frac{\gamma_a \pi \tan \theta}{\cos \theta} h_a^2 \quad (5)$$

And the corresponding adhesive force is:

$$F_a = -\frac{\gamma_a 2\pi \tan \theta}{\cos \theta} h_a \quad (6)$$

From the linear fit on Fig. 4b, γ_a is identified: $\gamma_a = 3.562 \text{ J m}^{-2}$.

In the same way as for other phenomena observed in this work, the influence of the adhesion is largely significant and should be considered in the modelling of nanoindentation testing of this material.

4. Modelisation and numerical simulations of nanoindentation tests

In this part, the modelling and the numerical simulation of nanoindentation test were carried out. The previous phenomena observed and identified experimentally were taken into account. The constitutive law of the materials will be identified macroscopically by experimental tests of compression. Then, the size effect will be modelled by a “zoning” coupled to an inverse analysis. A relevant choice of boundary condition will take into account the cohesion of the interface between the indenter and the material.

4.1. Macroscopic constitutive law

A constitutive law is identified from experimental compression tests realized at different constant strain rates (see Fig. 5). Friction between compression apparatus and sample is considered negligible. This allows interpreting the test as a pure uniaxial compression. Samples are assumed to be homogeneous and isotropic. An elasto-viscoplastic behaviour is considered. Rigorously, this blend is also viscoelastic but with a much lower sensitivity coefficient to the strain rate, evaluated at about 0.11 at room temperature, than for viscoplastic behaviour (Eq. (1) from Gaillard et al. (2013)).

Under these conditions, the measured Young's moduli are averaged to a value of 85 MPa. Poisson's ratio, ν , is

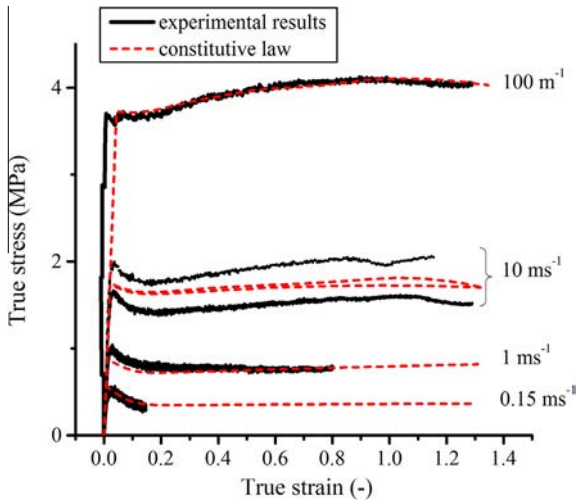


Fig. 5. Experimental stress–strain curve obtained from compression tests and corresponding deduced constitutive law.

estimated at 0.45 from video capture of the sample's deformation.

The viscoplastic behaviour of the material is modelled with an analytical function (Bucaille et al., 2002) comprising a part of power law type to describe the dependence to the strain rate and another part, called f , to describe the stress relaxation (yield drop) observed just after the plasticity activation, as follow:

$$\sigma(\varepsilon_p, \dot{\varepsilon}_p) = A(\varepsilon_p) \times \dot{\varepsilon}_p^{m_p(\varepsilon_p)} \times f(\varepsilon_p, \dot{\varepsilon}_p) \quad (7)$$

$$\text{with } \begin{cases} f(\varepsilon_p, \dot{\varepsilon}_p) \geq 1 & \text{if } \varepsilon_p < 0.2 \\ f(\varepsilon_p, \dot{\varepsilon}_p) \approx 1 & \text{if } \varepsilon_p \geq 0.2 \end{cases}$$

and where A and m_p are affine functions. The function f is defined by:

$$f(\varepsilon_p, \dot{\varepsilon}_p) = [1 + p(\dot{\varepsilon}_p) \exp(-q(\varepsilon_p - \varepsilon_0)^2)] \quad (8)$$

$$\text{with } \begin{cases} p = A_2 \dot{\varepsilon}_p^{m_2} \\ q, \varepsilon_0, A_2, m_2 \text{ constants} \end{cases}$$

An average maximal error of 8.4% was calculated on the value of the stress compared to the experimental values of compression tests. The identified parameters are reported in Table 1 and the law is compared to experimental curves on Fig. 5. Owing to compression tests which are realized with a strain rate between 0.15 and 100 ms^{-1} , nanoindentation tests which will be held in the following are between $\frac{h}{h_0} = 4$ and 400 ms^{-1} .

4.2. Implementation in ABAQUS

Finite element analysis was performed with the commercial software package ABAQUS 6.9. The problem was treated as being axisymmetric, following the concept of equivalent indenter shape (King, 1987; Bolshakov et al., 1995), and taking into account the tip radius of the tool considered rigid in this study. The mesh was adapted to different depths simulated. For small penetration ($h_{\text{max}} = 100 \text{ nm}$), the average size of elements is about 5 nm, for high penetration ($h_{\text{max}} = 4500 \text{ nm}$), average size of elements is around 100 nm. Fig. 6a shows the overall mesh for the problem and Fig. 6b shows a magnified view of the mesh close to contact surfaces. The geometry is meshed with 12033 elements and the complete problem has 13525 degrees of freedom. In the simulations one imposes the experimental evolution of the penetration depth, $h(t)$, versus time. A friction coefficient of 0.2 has been used.

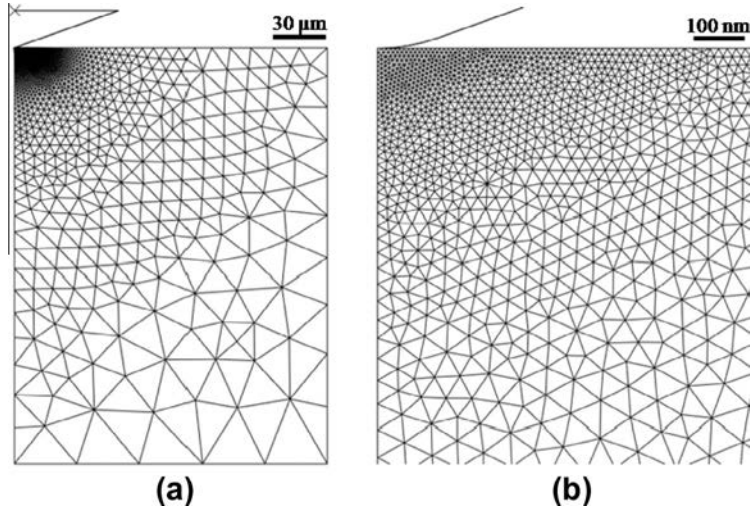
4.3. Loading and Indentation Size Effect (ISE)

The size effect corresponds to an evolution of the mechanical behaviour depending on the size of the deformed volume. However, during indentation test, the size of the deformed volume varies over the test as it depends directly of the penetration depth. So, the material behaviour varies in the same way. In order to simulate the size effect in nanoindentation tests, we proposed to discretize the material using a scaling “multi-zone” material driven by a finite number of experimental tests. In each zone, mechanical behaviour will be homogeneous, isotropic, constant and adapted in function of the size deformed

Table 1

Parameters of macroscopic constitutive law.

$A(\varepsilon_p)$ [MPa s ^{m_p}]	$m(\varepsilon_p)$ [-]	q [-]	ε_0 [-]	A_2 [-]	m_2 [-]
$2.1394 \varepsilon_p + 8.7248$	$0.0158 \varepsilon_p + 0.3684$	+0.7208	-0.075	1.6027	-0.4689

**Fig. 6.** (a) Overall mesh used for axisymmetric finite element modelling and (b) magnified view of the mesh close to the tip defect.**Table 2**Parameters extracted from the nanoindentation tests used for identifying the size effect at $\dot{h}/h = 0.04 \text{ s}^{-1}$.

N° test i	h_{\max} (nm)	F_{\max} (μN)	H_i (MPa)	X
1	115.8	31.8	70.9	15.8
2	211.8	64.1	47.7	10.6
3	584.1	184.2	19.7	4.4
4	1150.8	408.9	11.5	2.6
5	1578.7	743.7	11.2	2.5
6	2426.8	1639.8	10.6	2.3
7	4451.2	3554.4	6.8	1.5

volume. The position and the mechanical behaviour of each zone will be defined from the associated experimental nanoindentation test. This modelling is called “zoning”.

Even if this method does not allow explaining the physical origin of the ISE, the implementation of this zoning in the modelling allows at least to numerically reproduce the decrease of the hardness with the penetration depth. For this purpose, seven nanoindentation tests were realized at $\dot{h}/h = 0.04 \text{ s}^{-1}$, with maximal penetration (h_{\max}) evenly distributed between 115 nm and 4450 nm, and listed in Table 2.

We define the following notation where the subscript “∞” is added to the material properties corresponding to the macroscopic ones. Thereby, E_∞ and σ_∞ are macroscopic Young modulus and macroscopic yield strength, depending of ε_p and $\dot{\varepsilon}_p$, defined in paragraph §4.1. H_∞ is the macroscopic hardness measured by microhardness. In the same way, the subscript “ i ” allows to identify material properties associated with the test i . To lighten notation, terms E_i , σ_i

and H_i are regrouped under the term Mat_i . According to Eq. (1) (Section 3.2), $H_i = H_u$ was calculated for each test.

Given that the size effect corresponds to an evolution of the mechanical behaviour depending on the size of the deformed volume, we assumed that each material property is proportional to macroscopic property associated to a scale factor, called X_i , depending on size of the deformed volume during the test i . So, each material property can be defined as a function of the macroscopic material’s property and of the scale factor X_i .

$$Mat_i = f(Mat_\infty, X_i) \quad (9)$$

Knowing the evolution of hardness during the various tests, the scale factor X_i is defined by the following equation in function of H_i :

$$X_i = \frac{H_i}{H_\infty} \quad (10)$$

We also assumed that each individual mechanical property evolves similarly but not equally. So two coefficients, j and k , are introduced to define the scale factor related to elastic behaviour, defining E_i , and the one related to plastic behaviour, defining σ_i . In first approximation, j and k are considered constant. Equations are chosen to tend toward macroscopic properties when scale factor tend toward 1. So, elements of Mat_i were defined by the following equations:

$$\begin{cases} H_i = H_\infty \times X_i \\ E_i = E_\infty \times [j(X_i - 1) + 1] \\ \sigma_i = \sigma_\infty \times [k(X_i - 1) + 1] \end{cases} \quad \forall i \in \{1, 2, \dots, 7\} \quad (11)$$

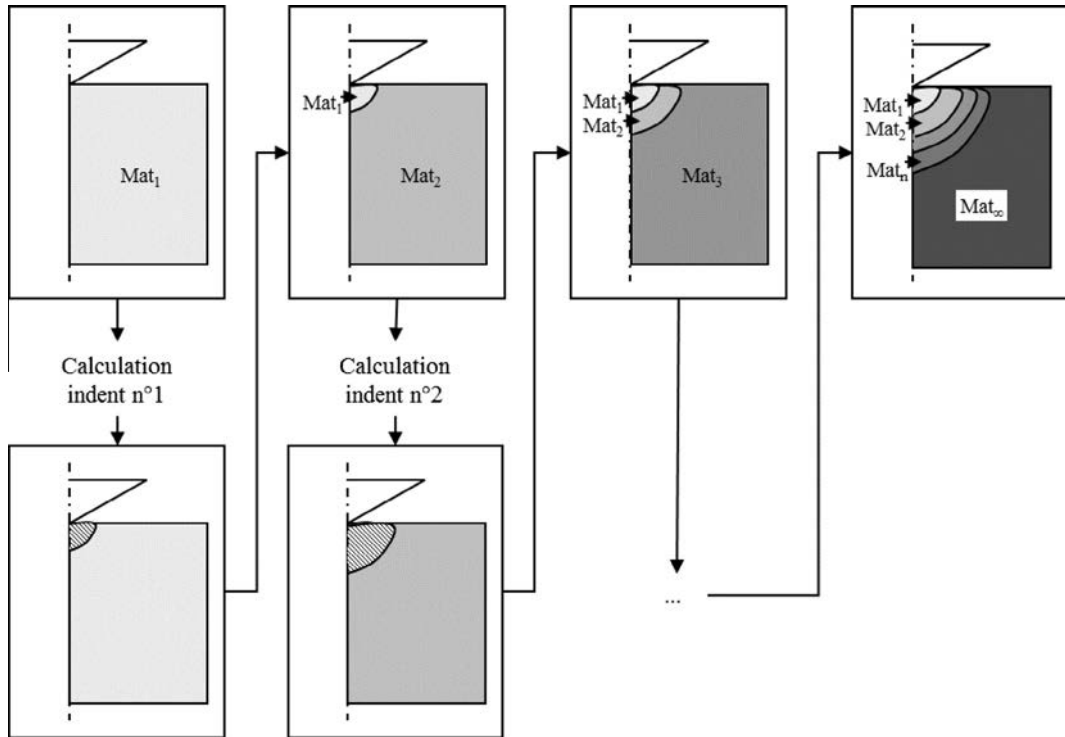


Fig. 7. Scheme of resolution for the calculation of the various zones used to account for the indentation size effect.

j and k will be identified by inverse analysis in the following.

Once the different behaviours of the material Mat_i defined, associated zones were identified with successive numerical simulation of each experimental test i , from shallowest to deepest indentations, using the method illustrated on Fig. 7.

For each simulation in ABAQUS, the experimental indentation depth versus time profile is used as indenter displacement instruction.

For the first calculation, corresponding to shallowest nanoindentation test, behaviour Mat_1 is applied to the entire part. Then, the plastically deformed zone is identified with a criterion on the plastic strain tensor for each element using a routine programmed in Python. In the following, the Mat_1 behaviour will be set for all elements identified in the first plastic deformed zone, called zone 1. For the second calculation, associated to the second nanoindentation test, the Mat_2 behaviour is applied to the entire part except elements from zone 1 (Mat_1). Test No. 2 is modelled and additional elements plasticised (apart those from zone 1) are defined as zone 2. In the following, the Mat_2 behaviour will be set for all elements of zone 2. For the next step, we impose Mat_3 behaviour to the entire piece excepted elements from zone 1 (Mat_1) and zone 2 (Mat_2). Test No. 3 is performed and zone 3 is identified in the same way as the previous. The process is repeated until the seven zones, related to the seven nanoindentation tests, are identified. After the last test, we apply the macroscopic behaviour (Mat_∞) to all elements that have not been

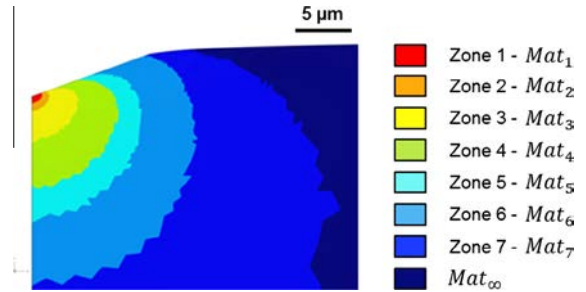


Fig. 8. Physical dimension of deformed zone.

plasticised during these 7 tests. Fig. 8 shows the result of the calculated zoning after a loading cycle.

Finally, only two coefficients had to be identified. Each couple (j, k) are identified by optimisation on the loading of the deeper indentation with a Gauss-Newton algorithm (least squares error), with, for each change of j or k , a recalculation of the corresponding zones. The coefficient related to the elastic behaviour and the one related to the plastic behaviour cannot be identified only on the loading sequence. So, the solution is not unique. A series of solution pairs are identified and are shown on Fig. 9. The pair solution is then determined with the unloading sequence.

4.4. Unloading and cohesion of interface

Once the different zones are identified and properties are set, for each pair solution, the calculation of the

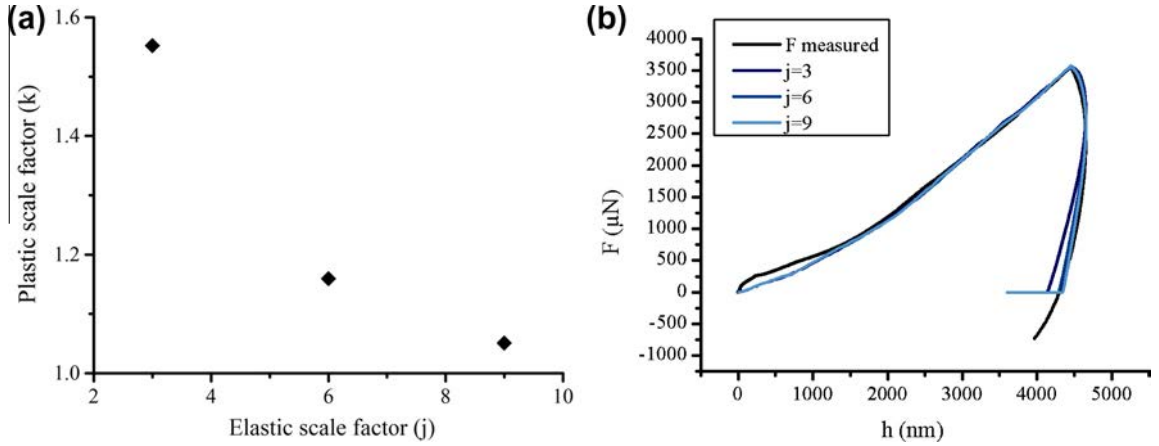


Fig. 9. (a) Series of pair solution identified defining the material properties and (b) loading and unloading cycle simulation for each pair solution (j, k).

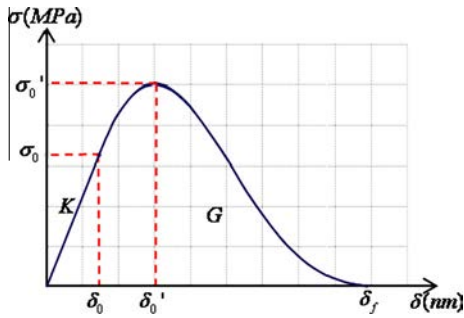


Fig. 10. Traction-separation behaviour with a failure mechanism used to account for the adhesive behaviour.

unloading is made by adding a law of cohesion on the interface between the indenter and the material to reproduce the tackiness of this interface. The law of cohesion was implemented by incorporating a cohesive zone model at the interface between indenter and material.

In ABAQUS, the features which allow the specification of generalised traction-separation behaviour for surfaces are defined as surface interaction properties. For simplicity, it was considered that the cohesive constraint is restricted to act along the contact in the normal direction only. So, pure normal separations, noted δ , give rise to cohesive forces, noted σ , in the normal direction. The available traction-separation model in ABAQUS assumes initially linear elastic behaviour followed by the initiation and evolution of damage of the interface. Damage was modelled to simulate the degradation and the eventual failure of the bonds between adhering surfaces. The failure mechanism consists of two factors: first a damage initiation criterion and secondly a damage evolution law. Once the damage initiation criterion is reached, i.e. the normal contact separation δ is superior to δ_0 , damage can occur according to the damage evolution law. The damage evolution law describes the rate at which the cohesive stiffness is degraded once the corresponding initiation criterion is reached. Wang et al. (Wang et al., 2004) use a triangular force-separation relationship for the user-defined interface

interaction elements. However, this relation has a singularity that is found in the simulation of the nanoindentation test. This singularity can be solved introducing a viscosity term in the constitutive cohesion law, as proposed by Xia et al. (Xia et al., 2007), or simply by choosing a law with continuous derivative as the one shown on Fig. 10 and defined by the following equations:

$$\begin{cases} \sigma = K\delta & \text{if } \delta \in [0; \delta_0] \\ \sigma = \alpha(1 - \frac{\delta}{\delta_f})^n (\frac{\delta}{\delta_f})^m & \text{if } \delta \in [\delta_0; \delta_f] \end{cases} \quad (12)$$

where σ is the nominal traction stress vector, defined as the cohesive forces acting along the contact in the normal direction divided by the current area at each contact point, δ is the contact-separation parameter, related to the displacement between the nodes on the slave surface and their corresponding projection points on the master surface along the contact normal, δ_0 is the value of the criterion which defines the initiation of the damage, δ_f is the value of the contact separation when the bonding force between surfaces fails, K is the initial cohesive stiffness and (α, n, m) are constants defining the force-separation law.

This cohesive law is then defined by 6 parameters. The continuity of the law and its derivative in $\delta = \delta_0$ reduces the number of constant to 4.

These 4 parameters defining the cohesive law, and the pair of parameters (j, k) defining the material properties presented previously, were then identified by inverse analysis on the unloading sequence of the nanoindentation

Table 3
Summary of the results obtained by inverse analysis.

Parameters	Calculated values
j	3
k	1.55
α	88.3 MPa
δ_f	350 nm
m	1.23
n	1.64
δ_0	42.6 nm
K	126500 MPa m ⁻¹

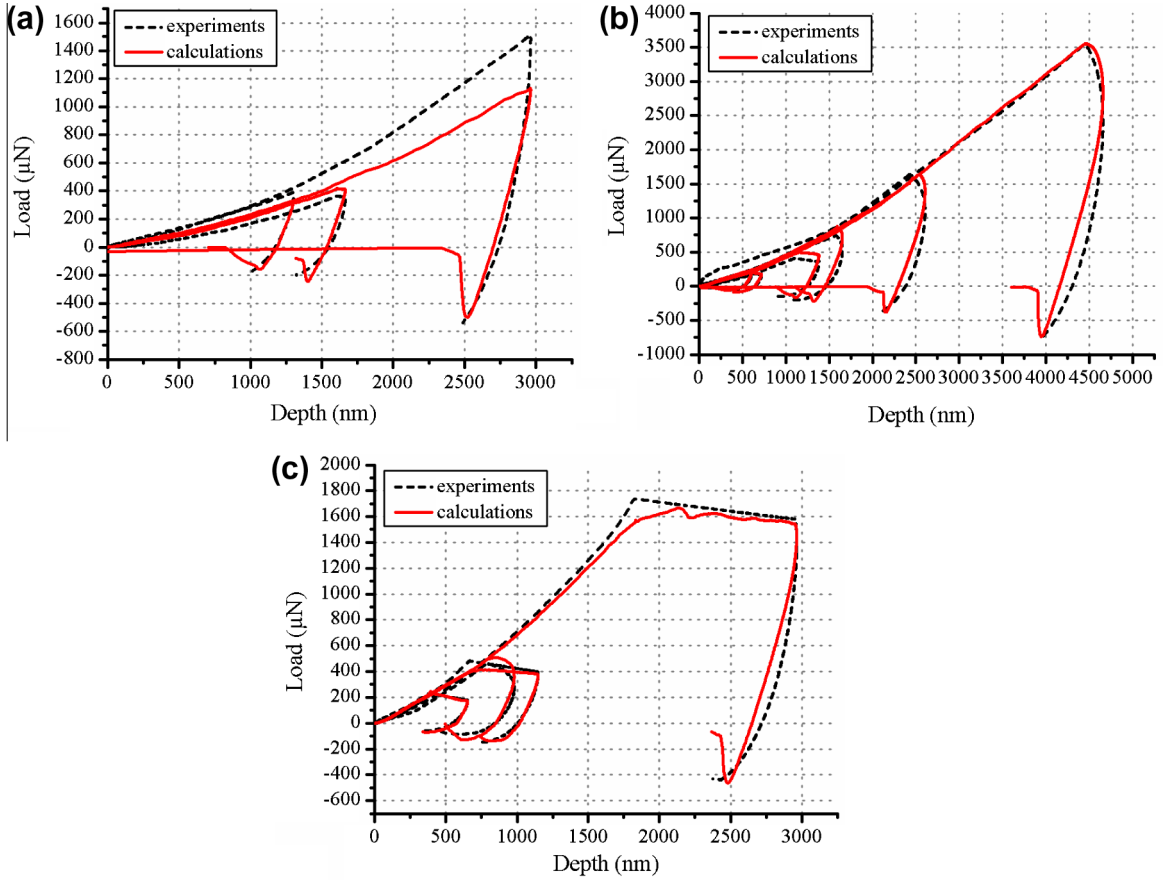


Fig. 11. Comparison between different experimental nanoindentation tests and corresponding numerical calculations: (a) $\frac{\dot{h}}{h} = 0.004 \text{ s}^{-1}$, (b) $\frac{\dot{h}}{h} = 0.04 \text{ s}^{-1}$ and (c) $\frac{\dot{h}}{h} = 0.4 \text{ s}^{-1}$.

simulation. The results of this identification procedure are summarized in Table 3.

5. Discussion

As a first approximation, it was assumed that $h \approx h_c$. So we were able to highlight the size effect in nanoindentation (Fig. 3) and to identify it with Eq. (10). Then a model of material behaviour in nanoindentation, performed at a given strain rate, was developed (Eq. (12)) from the previous identified parameters and using inverse analysis. The resulting load-penetration curves are in good agreement with the experimental ones. Then the identified parameters have been used to simulate the experiments performed at other values of the strain rate. The agreements appear to be also acceptable (Fig. 11). So this approximation does not challenge the interpretation of the nanoindentation results.

The agreement is good in all steps of the experiments: loading and unloading till the maximal separation force. It means that the cohesive zone model with relevant values of its related parameters is able to represent the tackiness of this material. The study of the contact surface during the unloading segment of nanoindentation allows to highlight different behaviours depending on the depth

of penetration. The loss of contact is more abrupt for deep indents than for shallow indents. In the latter case, the propagation of the crack, reducing the contact surface between the indenter and the material, is more gradual. These results are visible in Fig. 11. Experimental results validate clearly this phenomenon. The outcomes of the numerical simulation corroborate the corresponding experimental measurements. One can notice the good agreement in the shape of the unloading curve and in the level of loss of contact between the indenter and the surface.

Moreover the cohesive model used is consistent with the thermodynamic work of adhesion measured experimentally in §3.3 (3.56 J m^{-2}). Indeed, the calculated surface energy from cohesive model, deduced from the integration of Eq. (12), gives 2.6 J m^{-2} .

For identifying the mechanical properties of the blend in nanoindentation, the thermal effects on the plastic deformation were neglected. It appears at first sight as a limitation of this work because one can expect that the mechanical properties of this material are very sensitive to the temperature variations. In fact at room temperature the rosin fraction contained in this blend is close to its glass transition. However this effect is probably small. During the indentation tests, the low dissipation and the high

thermal conductivity of the indenter assure no significant heating of the indented material. This conclusion is confirmed by the fact that experiments and numerical simulations for various strain rates are very similar.

6. Conclusion

Experimental tests of nanoindentation realised on bio-sourced adhesive, i.e. 75% rosin/25% beeswax, reveal a very complex mechanical behaviour. In fact, this material exhibits a high dependency to strain rate (mainly viscoplastic), tack properties but also a large indentation size effect. Results of compression tests were used in order to provide a macroscopic constitutive law and its sensitivity to strain rate. Based on these experimental observations, nanoindentation tests on this material were modelled and simulated numerically in order to assess the tack properties of the material. A cohesive zone model was used to represent the adhesive behaviour, and a zoning to account for size effects in indentation test (ISE). Unfortunately, it does not explain the physical origin of ISE. Nevertheless the zoning presented here appears to be a practical and original way to account for the evolution of the mechanical properties with the size of the deformed volume during the indentation. Parameters of the different models were identified by inverse analysis. Indeed, the complicated mechanical behaviour under instrumented indentation of this bio-sourced adhesive made of a elasto-viscoplastic blend is relatively well described by the finite element model proposed here. In fact, the experimental results and numerical computations are in good agreement for various values of penetration depths and different strain rates. Finally, this paper shows that nanoindentation experiments, today quite easy to implement, often require post-treatment and complex analyses in order to assess understandable physical or mechanical properties.

Acknowledgment

This work was supported by Carnot-Mines.

References

Giri, M., Bousfield, D.B., Unertl, W.N., 2001. Dynamic contacts on viscoelastic films: work of adhesion. *Langmuir* 17, 2973–2981.

Yang, F., 2002. Adhesive contact between a rigid axisymmetric indenter and an incompressible elastic thin film. *J. Phys. D Appl. Phys.* 35, 2614–2620.

Sirghi, L., Rossi, F., 2006. Adhesion and elasticity in nanoscale indentation. *Appl. Phys. Lett.* 89, 243118.

Ebenstein, D.M., Pruitt, L.A., 2006. Nanoindentation of biological materials. *Nano Today* 3, 26–33.

Sneddon, I.N., 1965. The relation between load and penetration in the axisymmetric Boussinesq problem for a punch of arbitrary profile. *Int. J. Eng. Sci.* 3, 47–57.

Pharr, G.M., Oliver, W.C., Brotzen, F.R., 1992. On the generality of the relationship among contact stiffness, contact area, and elastic modulus during indentation. *J. Mater. Res.* 7, 613–617.

King, R.B., 1987. Elastic analysis of some punch problems for a layered medium. *Int. J. Solids Struct.* 23, 1657–1664.

Oliver, W.C., Pharr, G.M., 1992. Improved technique for determining hardness and elastic modulus using load and displacement sensing indentation experiments. *J. Mater. Res.* 7, 1564–1583.

Bolshakov, A., Oliver, W.C., Pharr, G.M., 1995. An explanation for the shape of nanoindentation unloading curves based on finite element simulation. *Mater. Res. Soc. Symp. Proc.* 356, 675–680.

Jonhson, K.L., Kendall, K., Roberts, A.D., 1971. Surface energy and the contact of elastic solids. *Proc. R. Soc. London A* 324, 301–313.

Barthel, E., 2008. Adhesive elastic contacts: JKR and more. *J. Phys. D Appl. Phys.* 41, 163001.

Barthel, E., Fretigny, C., 2009. Adhesive contact of elastomers: effective adhesion energy and creep function. *J. Phys. D Appl. Phys.* 42, 195302.

Barthel, E., Perriot, A., 2007. Adhesive contact to a coated elastic substrate. *J. Phys. D Appl. Phys.* 40, 1059–1067.

Mary, P., Chateauminois, A., Fretigny, C., 2006. Deformation of elastic coatings in adhesive contacts with spherical probes. *J. Phys. D Appl. Phys.* 39, 3665–3673.

Argatov, I., 2010. Frictionless and adhesive nanoindentation: asymptotic modeling of size effects. *Mech. Mater.* 42, 807–815.

Ji, H., Robin, E., Rouxel, T., 2009. Compressive creep and indentation behavior of plasticine between 103 and 353K. *Mech. Mater.* 41, 199–209.

Kameda, T., 2005. ¹³C solid-state NMR analysis of heterogeneous structure of beeswax in native state. *J. Phys. D Appl. Phys.* 38, 4313–4320.

Jablonski, P., Golloch, A., Borchard, W., 1999. DSC-measurements of amber and resin samples. *Thermochim. Acta* 333, 87–93.

Morgan, J., Townley, S., Kemble, G., Smith, R., 2002. Measurement of physical and mechanical properties of beeswax. *Mater. Sci. Technol.* 18, 463–467.

Prevost, T.P., Jin, G., de Moya, M.A., Alam, H.B., Suresh, S., Socrate, S., 2011. Dynamic mechanical response of brain tissue in indentation *in vivo*, *in situ* and *in vitro*. *Acta Biomater.* 7, 4090–4101.

Kasapis, S., Sablani, S.S., 2005. A fundamental approach for the estimation of the mechanical glass transition temperature in gelatin. *Int. J. Biol. Macromol.* 36, 71–78.

Qian, X.Q., Cao, Y.P., Zhang, J.Y., Raabe, D., Yao, Z.H., Fei, B.J., 2008. An inverse approach to determine the mechanical properties of elastoplastic materials using indentation tests. *CMC Comput. Mater. Con.* 7 (1), 33–41.

Qasmi, M., Delobelle, P., Richard, F., Brun, C., Fromm, M., 2004. Viscoelastic mechanical properties determined by nanoindentation tests and its numerical modelling of polypropylene modified by He+ particle implantation and e(−) irradiation. *Prog. Org. Coat.* 51 (3), 195–204.

Keerthika, B., Cao, Y.P., Raabe, D., 2009. Mechanical characterization of viscoelastic-plastic soft matter using spherical indentation 10 (3), 243–258.

<http://www.arizonachemical.com/Products/Adhesive-Resins/Rosin-Esters/> (16/05/2013).

http://www.eastman.com/Markets/Tackifier_Center/Tackifier_Families/Rosin_Resins/Pages/Rosin_Esters.aspx (16/05/2013).

Gaillard, Y., Mija, A., Burr, A., Darque-Ceretti, E., Felder, E., Sbirrazzuoli, N., 2011. Green material composites from renewable resources: polymorphic transitions and phase diagram of beeswax/rosin resin. *Thermochim. Acta* 52, 90–97.

Gaillard, Y., Girard, M., Burr, A., Darque-Ceretti, E., Felder, E., 2013. Superplastic behaviour of rosin/beeswax blends at room temperature. *J. Appl. Polym. Sci.* 128, 2713–2719.

<http://ets-leygonie.net/> (16/05/2013).

Briscoe, B.J., Fiori, L., Pelillo, E., 1998. Nano-indentation of polymeric surfaces. *J. Phys. D Appl. Phys.* 31, 2395–2405.

Oliver, W.C., Pharr, G.M., 2004. Measurement of hardness and elastic modulus by instrumented indentation: advances in understanding and refinements to methodology. *J. Mater. Res.* 19, 3–20.

Nikolov, S., Han, C.S., Raabe, D., 2007. On the origin of size effects in small-strain elasticity of solid polymers. *Int. J. Solids Struct.* 44, 1582–1592.

Han, C.S., Nikolov, S., 2007. Indentation size effects in polymers and related rotation gradients. *J. Mater. Res.* 22, 1662–1672.

Dorset, D.L., 1999. Development of lamellar structures in natural waxes-an electron diffraction investigation. *J. Phys. D Appl. Phys.* 32, 1276–1280.

Tatiraju, R., Han, C.S., Nikolov, S., 2008. Size dependent hardness of polyamide/imide. *Open Mech. J.* 2, 89–92.

Yang, F., 2006. Effect of adhesion energy on the contact stiffness in nanoindentation. *J. Mater. Res.* 21, 2683–2688.

Bucaille, J.L., Felder, E., Maur, S., 2002. Identification of the viscoplastic behavior of a polycarbonate based on experiments and numerical modeling of the nano-indentation test. *J. Mater. Sci.* 37, 3999–4011.

Abaqus 6.9 Documentation.

Wang, M., Liechti, K.M., White, J.M., Winter, R.M., 2004. Nanoindentation of polymeric thin films with an interfacial force microscope. *J. Mech. Phys. Solids* 52, 2329–2354.

Xia, S.M., Gao, Y.F., Bower, A.F., Lev, L.C., Cheng, Y.T., 2007. Delamination mechanism maps for a strong elastic coating on an elastic-plastic substrate subjected to contact loading. *Int. J. Solids Struct.* 44, 3685–3699.